# Tunnelling around bends - wave scattering in curved shell structures

Neekar M Mohammed[a,b,*], Stephen C Creagh[a], Gregor Tanner[a]

[a] *School of Mathematical Sciences, University of Nottingham, United Kingdom*
[b] *Department of Mathematics, College of Science, University of Sulaimani, Sulaymaniyah, Kurdistan Region, Iraq*

**Abstract**

A ray dynamics describing wave transport on curved and smooth thin shells can be obtained from the underlying wave equations via the Eikonal approximation. We analyse mid-frequency effects near the ring frequency for curved plates consisting of a cylindrical region smoothly connected to two flat plates. Using classical shell theory, we treat a corresponding ray-tracing limit derived in the short wavelength regime for bending, shear and pressure incident waves. A treatment based on real rays gives either total reflection or total transmission; the solution of the full wave equations shows in contrast a smooth transition and exhibits resonant states localized in and around the region of maximal curvature. We show here for the first time, that both the smooth transition from total reflection to total transmission and the occurrence of resonant states can be described in a ray tracing approximation by extending the treatment to complex rays. In this sense, wave transmission across bends is a tunnelling phenomenon similar to the tunnelling effects known in optics and quantum mechanics. Based on simplified graph models, we can make qualitative predictions for resonance positions in parameter and frequency spaces. We are thus able to approximate the scattering matrix for waves incident on the bend accounting for tunnelling mediated by resonant states and uniformly treating the transition between the limits of totally reflected and totally transmitted waves.

*Keywords:* Elastic waves in shells, wave asymptotics, ray-tracing, resonant tunnelling, reflection and transmission coefficients.

## 1. Introduction

Modelling the vibroacoustic response of mechanical systems is a challenging task, especially for large complex mechanical built-up structures in

*Corresponding author
*Email address:* neekar.mohammed@nottingham.ac.uk (Neekar M Mohammed )

the mid-to-high frequency regime. At low-frequencies, with wavelengths comparable to the size of the structure, standard modelling tools such as finite and boundary element methods are used routinely; these methods are, however, not scalable to ever higher frequencies due to the prohibitive increase in model size. High-frequency methods such as ray-tracing may be employed in this limit and are used extensively in three-dimensional wave problems such as in acoustics, electromagnetism and optics. Only recently, attempts to implement ray-tracing ideas for structure-borne sound have been considered. In particular, ray-tracing on complex built-up structures has been implemented using the so-called Dynamical Energy Analysis (DEA) [1] describing wave transport in the high-frequency limit. This method has been formulated on meshes [2] and is based on local ray-tracing approximations with ray trajectories moving along straight lines in each mesh segment. DEA can thus estimate the flow of vibrational energy in shell structures of arbitrary complexity such as full body-in-blue vehicles [3]. The implementation of curvature corrections in a DEA treatment based on meshed shell structures has been discussed in [4]. Here, the local ray dynamics are approximated using piecewise straight line segments including back reflections which can lead to distortions for moderately curved shells (with radius of curvature comparable to the wavelength). Improvements on this rather ad-hoc approach have been reported in [5, 6]. We will revisit and extend these results in this paper.

Starting from the general equations for thin shells of arbitrary curvature, a well-known approach to describe ray dynamics for bending and in-plane waves is due to Pierce [7], obtained by deriving a local dispersion relation for different wave modes in the short wavelength regime. In the special case of shells being homogeneous and thin, somewhat simpler dispersion relations have been derived by Norris and Rebinsky [8] which will form the basis of our work. Asymptotic techniques describing the wave dynamics in thin walled shells have also been discussed in a book by Mikhasev and Tovstik [9] with particular attention given to the modified Wentzel-Kramers-Brillouin (WKB) method. Different asymptotic regimes for the dynamics of curved shells have been considered by Kaplunov *et al.* [10] as well as Babich and Kiselev [11].

Following [8], we deduce a ray dynamics by interpreting the dispersion curves as the contour lines of a Hamilton function from which Hamilton's equations of motion for the rays are obtained. These equations depend – along with material parameters and the thickness – on the local radii of curvature. The ray solutions are in general not straight lines and may encounter turning points or caustics: that is, the curvature profile of the shell may act as a barrier. In a process that is analogous to tunnelling of a quantum particle through a potential energy barrier [12], partial reflection from or transmission through such curvature barriers may arise and is similarly treated here using complex solutions of the ray equations: calculation of

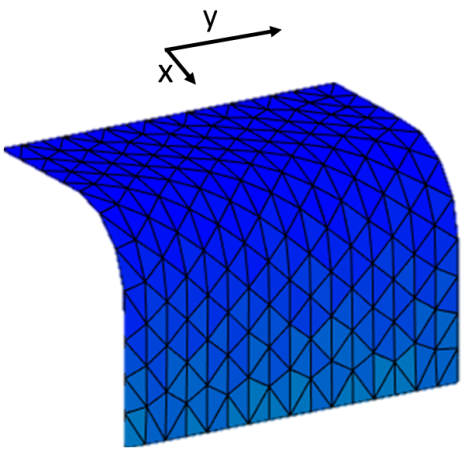


Figure 1: A quarter cylindrical ridge connected to flat plates on either side equivalent to the structure considered in [6].

such curvature tunnelling is the focus of the paper.

For the sake of simplicity and following [5, 6], we will study the ray and wave dynamics for a particular example – two plates joined by curved section with a specified curvature profile along the circumferential direction as shown in Fig. 1. This assumed geometry simplifies the analysis by making the problem have one effective degree of freedom. We also concentrate on incident waves that are of bending type: in the parameter regimes we consider, these do not couple significantly to in-plane modes and, having the shorter wavelength, are more appropriately treated by ray techniques. In a pure ray-tracing picture, incident rays approaching the curved region of the plate are either totally reflected or totally transmitted, depending on the angle of incidence. However, the solutions of the full wave equations show a smooth, wavelength-dependent transition between total reflection or transmission, interspersed with resonance states. This was also observed in [6], but not treated ray-dynamically.

In the context of quantum mechanics, such tunnelling effects are well established [12] and can be understood using a range of approximation techniques, based on extending ray dynamics to complex coordinates. The aim of this paper is to extend such complex ray theory to the scattering of bending waves in a curved shell. For problems with several degrees of freedom, the use of complex solutions of ray dynamics to treat tunnelling phenomena remains a challenging problem that may require extension of chaotic dynamics to the complex domain (see [13, 14], for example) or show behaviour associated with coupling between complex orbits and and chaotic [15] or resonant structures [16] typical of nonintegrable Hamiltonian systems (and see [17, 18] for other aspects of multidimensional tunnelling). In this paper we treat problems that are globally integrable and

therefore the topology of complex solutions can be explicitly described, allowing simpler analytical approximation [19] of the tunnelling features observed. However it should be noted that for more general shell geometries all the complexity of generic multidimensional tunnelling problems [17, 18] can arise.

The paper is structured as follows. In Sec. 2 we briefly introduce the dispersion curves used to characterise ray dynamics on a cylindrical shell, describe the curvature profiles to be used in numerical illustrations and describe the basic assumptions of the WKB approximation, along with defining scaled, dimensional variables which make small and large parameters evident. In Sec. 3, we devise a model for resonant tunnelling based on a graph approach, and the theory for incorporating the relevant complex orbits into approximation of reflection and transmission amplitudes is discussed. Explicit numerical illustrations of the theory are offered in Sec. 4, comparing the WKB approach with full wave calculations, while conclusions are given in Sec. 5.

## 2. Thin Shell Theory, Short Wavelength Asymptotics and Ray Dynamics

Numerous thin-shell theories have been derived to determine the dynamic and vibro-acoustic behavior of thin-shell structures. These include Donnell's theory [20] and generalisations thereof [7, 21]; for more details also about other approaches, see the book by Leissa [22] and a review article by Qatu [23]. The calculations in this paper are based on Donnell's shell theory, which is discussed in more detail by Pierce [7], and Norris and Rebinsky [8]. In particular, we follow Søndergaard *et al.* [5, 6], who have applied this approach to the case of an isotropic, cylindrical shell. The work of [5, 6] has used thin-shell models to incorporate curvature effects in ray-tracing models, which we extend in this paper to include wave features such as evanescent corrections and resonant tunnelling.

### *2.1. Wave model for thin shells*

We consider the case of a cylindrical shell extending to $\pm\infty$ in the $y$ direction and a varying radius of curvature $R(x)$ in the circumferential $x$ direction such as, for example, shown in Fig. 1. The thickness of the shell is $h$, its (volume-) density $\rho$ with Poisson ratio $\nu$ and Young's modulus $E$. It is assumed that the shell is thin, so that in particular $h \ll R$ (see Sec. 2.3 for more detail about assumed small and large parameters). We let $\mathbf{x} = (x, y)$ denote curvilinear coordinates on the shell, where $y$ is a coordinate along the cylindrical axis of the structure and $x$ is an arc length perpendicular to it. The displacement of a point originally on the reference surface within the shell is denoted by $\mathbf{u}(x, y, t) = [u(x, y, t)\ v(x, y, t)\ w(x, y, t)]$. The simplified shell theory presented in [6] reduces the elastic equations to the following

set of partial differential equations,

$$\begin{aligned}
\frac{1}{c_P^2}\frac{\partial^2 u}{\partial t^2} &= \frac{\partial^2 u}{\partial x^2} + \frac{(1+\nu)}{2}\frac{\partial^2 v}{\partial x \partial y} + \frac{(1-\nu)}{2}\frac{\partial^2 u}{\partial y^2} + \frac{\partial}{\partial x}(\kappa(x) w) \\
\frac{1}{c_P^2}\frac{\partial^2 v}{\partial t^2} &= \frac{\partial^2 v}{\partial y^2} + \frac{(1+\nu)}{2}\frac{\partial^2 u}{\partial x \partial y} + \frac{(1-\nu)}{2}\frac{\partial^2 v}{\partial x^2} + \nu\kappa(x)\frac{\partial w}{\partial y} \\
\frac{1}{c_P^2}\frac{\partial^2 w}{\partial t^2} &= -\frac{B}{C}\Delta^2 w - \kappa(x)\left(\frac{\partial u}{\partial x} + \nu\frac{\partial v}{\partial y} + \kappa(x) w\right),
\end{aligned} \tag{1}$$

where

$$B = \frac{Eh^3}{12(1-\nu^2)} \quad \text{and} \quad C = \frac{Eh}{1-\nu^2}$$

denote the bending and extensional stiffnesses and

$$c_P^2 = \frac{C}{\rho h} = \frac{E}{\rho(1-v^2)}$$

is the pressure wave velocity, while $\kappa(x)$ denotes the local curvature in the $x$ direction.

We take advantage of the translational symmetry in the $y$ direction to seek wave solutions in the form

$$\mathbf{u}(x, y, t) = \hat{\mathbf{u}}(x) \mathrm{e}^{\mathrm{i}k_y y - \mathrm{i}\omega t}, \tag{2}$$

where the wavenumber component $k_y$ and the frequency $\omega$ are constants and $\hat{\mathbf{u}} = (\hat{u}, \hat{v}, \hat{w})^T$. Substituting the ansatz (2) into the PDE system (1) and denoting $k_P = \omega / c_P$ leads to the following system of ODE's in the variable $x$:

$$\frac{\mathrm{d}^2\hat{u}}{\mathrm{d}x^2} + \left(k_P^2 - \frac{(1-v)}{2}k_y^2\right)\hat{u} + \mathrm{i}k_y\frac{(1+v)}{2}\frac{\mathrm{d}\hat{v}}{\mathrm{d}x} + \frac{\mathrm{d}}{\mathrm{d}x}\left(\kappa(x)\hat{w}\right) = 0 \tag{3a}$$

$$\frac{(1-v)}{2}\frac{\mathrm{d}^2\hat{v}}{\mathrm{d}x^2} + \left(k_P^2 - k_y^2\right)\hat{v} + \mathrm{i}k_y\left(\frac{(1+v)}{2}\frac{\mathrm{d}\hat{u}}{\mathrm{d}x} + \nu\kappa(x)\hat{w}\right) = 0 \tag{3b}$$

$$\frac{B}{C}\left(\frac{\mathrm{d}^4\hat{w}}{\mathrm{d}x^4} - 2k_y^2\frac{\mathrm{d}^2\hat{w}}{\mathrm{d}x^2} + k_y^4\hat{w}\right) + \left(\kappa^2(x) - k_P^2\right)\hat{w} + \kappa(x)\left(\frac{\mathrm{d}\hat{u}}{\mathrm{d}x} + \mathrm{i}\nu k_y\hat{v}\right) = 0 \tag{3c}$$

*2.2. Eikonal approximation for thin shells*

Next, we look for approximate solutions to these ODE's in WKB form,

$$\hat{\mathbf{u}}(x) = \mathbf{a}(x)\mathrm{e}^{\mathrm{i}S(x)}, \tag{4}$$

where the components of $\mathbf{a} = [a_u,\ a_v,\ a_w]^T$ are the amplitudes in the in-plane directions $x$ and $y$ and in the direction normal to the shell, respectively. The gradient of the phase function $S(x)$ defines a local wavenumber in the $x$ direction

$$k_x(x) = \frac{\mathrm{d}S}{\mathrm{d}x}. \tag{5}$$

All of these amplitude and phase functions depend parametrically on $k_y$ and $\omega$, although these dependencies have been suppressed in our notation. Note that in order to treat evanescence effects in the wave transport problem, we must allow the phase function $S(x)$ to be complex-valued as discussed in following sections.

For simplicity of notation, we have not explicitly identified a large parameter in our notation so far, but the Eikonal expansion to follow assumes that the length scale over which the curvature changes is much greater than the typical local wavelength. We correspondingly impose that $\mathbf{a}(x)$ varies over these longer length scales. Note that for simple smooth curvature profiles over which the bending angle is $O(1)$, this longer length scale can be effectively identified with the minimum radius of curvature, but the Eikonal expansion fails when the curvature changes rapidly, even if the radius of curvature itself remains large.

Substituting the ansatz (4) into the equations of motion (3) and neglecting terms containing derivatives in $\mathbf{a}$, (thus assuming that the amplitudes $\mathbf{a}$ vary slowly along $x$ compared to $S(x)$), we deduce that $k_x$ must satisfy an Eikonal equation of the form

$$D(x, k_x; k_y, \omega) = 0,$$

where the function $D(x, k_x; k_y, \omega)$ is defined by

$$\begin{aligned} D(x, k_x; k_y, \omega) &= \begin{vmatrix} k_x^2 + \dfrac{1-\nu}{2}k_y^2 - k_P^2 & \dfrac{1+\nu}{2}k_x k_y & -\mathrm{i}\kappa(x)k_x \\ \dfrac{1+\nu}{2}k_x k_y & k_y^2 + \dfrac{1-\nu}{2}k_x^2 - k_P^2 & -\mathrm{i}\nu\kappa(x)k_y \\ -\mathrm{i}\kappa(x)k_x & -\mathrm{i}\nu\kappa(x)k_y & k_P^2 - \kappa^2(x) - \dfrac{B}{C}k^4 \end{vmatrix} \\ &= \left(k_P^2 - \frac{1}{2}k^2(1-\nu)\right)\left(\left(k_P^2 - k^2\right)\left(k_P^2 - \frac{Bk^4}{C}\right) - k_P^2\kappa^2(x)\right) \\ &\quad + (1-\nu^2)\kappa^2(x)k_y^2\left(k_P^2 - \frac{1}{2}(1-\nu)k_y^2\right), \end{aligned} \tag{6}$$

and $k^2 = k_x^2 + k_y^2$. It should be emphasized that the asymptotic treatment here is a short wavelength approximation, that is, the local wavenumber is substantially larger than the reciprocal of the length scales over which the curvature radii change. For a treatment of the low-frequency, long wavelength asymptotics, see [10].

The secular equation (6) provides a dispersion relation for modes propagating in curved plates and can be interpreted as a Hamilton function for an underlying ray dynamics. The method of characteristics leads to equations of motion of the form

$$\dot{x} = \frac{\partial D}{\partial k_x}, \tag{7a}$$

$$\dot{k}_x = -\frac{\partial D}{\partial x}, \tag{7b}$$

describing a ray dynamics for energy transport on curved and homogeneous smooth thin shells.

The Hamiltonian (6) provided the basis for the work in [5, 6] and accounts for ray dynamics of both bending and in-plane waves at sufficiently high frequencies. For moderate curvature, each of these modes locally defines a separate level set of $D(x, k_x; k_y, \omega) = 0$ (see Fig. 3, discussed in Sec. 2.4). The ratio of radius of curvature to plate thickness provides a second large parameter, independent of frequency. This second large parameter can be exploited to use ray equations for bending modes even for moderate frequencies for which the wavelength of in-plane modes is not particularly small in comparison with the length scales of the curved region. In this second regime we find nontrivial deflection of rays associated with the bending mode, which is the focus of the rest of this paper. In order to describe the regime we need a more systematic treatment of the large and small parameters in the problem, which we provide in the next subsection by defining scaled variables.

### *2.3. Scaled variables*

In order to more formally identify small and large parameters behind the Eikonal expansion, we define scaled variables. We start by choosing a length scale $L$ characteristic of the problem: a convenient choice would be the minimum radius of curvature achieved over the curved section of the shell. Then the scaled plate thickness

$$H = \frac{h}{L} \tag{8}$$

is a natural small parameter for the problem. Note that since $h \ll R$ is a necessary condition for the thin shell equations (1) to hold in the first

place, we implicitly assume that $H \ll 1$ throughout this work. We define corresponding scaled coordinates and curvature profile

$$X = \frac{x}{L}, \qquad Y = \frac{y}{L} \quad \text{and} \quad \mathcal{K}(X) = L\kappa(x)$$

along with the scaled wavenumber variables

$$K_x = Lk_x, \qquad K_y = Lk_y \quad \text{and} \quad K = Lk.$$

We also define a scaled frequency

$$\Omega = \frac{L\omega}{c},$$

where $c = \sqrt{E/\rho}$, and the following scaled wavenumbers

$$K_P = Lk_P = \sqrt{1-\nu^2}\Omega, \quad K_S = \sqrt{2(1+\nu)}\Omega, \quad K_B = (12(1-\nu^2))^{1/4}\sqrt{\frac{\Omega}{H}},$$

respectively, characterising pressure, shear and bending modes in the flat limit.

Then the Hamiltonian (6) can, after scaling by a constant factor, be written in terms of these scaled parameters and variables in the following form

$$\begin{aligned} D'(X, K_x; K_y, \Omega) =& (K^2 - K_S)^2 (K^2 - K_P^2)(K_B^4 - K^4) \\ &+ \frac{12}{H^2}\mathcal{K}^2(X)\left[K_P^2(K^2 - K_S^2) - (1-\nu^2)K_y^2(K_y^2 - K_S^2)\right]. \end{aligned} \tag{9}$$

Having identified $H = h/L$ as a natural small parameter, in terms of which $\mathcal{K} = O(1)$, we concentrate in the rest of this paper on a frequency regime such that

$$\Omega = O(1).$$

Then the in-plane, scaled wavenumbers are similarly such that

$$K_P = O(1) \quad \text{and} \quad K_S = O(1),$$

while the scaled bending wavenumber

$$K_B = O\left(\frac{1}{\sqrt{H}}\right)$$

is a large parameter.

We also focus in the following on bending waves whose angle of incidence is such that $K_y \sim K \sim K_B = O(1/\sqrt{H})$: then there is no significant

coupling to in-plane modes through the curved section of the plate. In this case the scaled Hamiltonian can be approximated at leading order by

$$D'(X, K_x; K_y, \Omega) = D''(X, K_x; K_y, \Omega)\left(1 + O\left(\frac{1}{H}\right)\right),$$

where

$$D''(X, K_x; K_y, \Omega) = K^4(K_B^4 - K^4) - \frac{\mathcal{K}^2(X)}{\Omega^2} K_B^4 K_y^4 \tag{10}$$

and assuming that the scaled curvature is $\mathcal{K}(X) = O(1)$ in the region of maximum curvature of the plate. Then the terms remaining in $D''(X, K_x; K_y, \Omega)$ are both of $O(K_B^8) = O(1/H^4)$ for bending waves in the curved region, so there is significant deflection of rays there.

### *2.4. Models of shell geometry and dispersion curves*

We now set out explicit examples of dispersion relations obtained from (9). For illustrations of the ray picture we consider a family of curvature functions previously used in [6], albeit with different parameter values, chosen here so that the problem behaves generically around the critical case between total transmission and total reflection of rays. By choosing as the length scale $L$ the minimum radius of curvature over the curved region, these are in scaled coordinates of the form

$$\mathcal{K}(X) = \frac{f(X)}{f(0)}, \tag{11}$$

where

$$f(X) = \frac{1}{2}\left(\mathrm{erf}\left(\frac{X + X^*}{\delta X}\right) - \mathrm{erf}\left(\frac{X - X^*}{\delta X}\right)\right), \tag{12}$$

with the parameters $X^*$ and $\delta X$ respectively controlling the location at which the shell transitions from flat to curved, and the sharpness of that transition.

Fig. 2 shows three different curvature profiles used in this paper, as a function of real $X$ in part (a) and as $X$ moves along the imaginary axis in part (b): this latter aspect is relevant to the discussion of complex rays in later sections. Going from the blue to the red to the black curve, the profile (as a function of real $X$) transitions from a generic quadratic maximum, Gaussian-like in shape, to one with sharper transition and a rather flat maximum. In all cases, we have $\mathcal{K}(X) \to 0$ in the asymptotic flat regions $X \to \pm\infty$ and the maximum curvature $\mathcal{K}_{\max} = 1$ is achieved at $X = 0$. The area under each of the curves in Fig. 2 is the total angle over which the plate bends through the curved region. In all the examples, the two flat regions of the plate are perpendicular to each other: that is, all curvature profiles in Fig. 2 have been fixed to have an area under the curve equal to $\pi/2$.

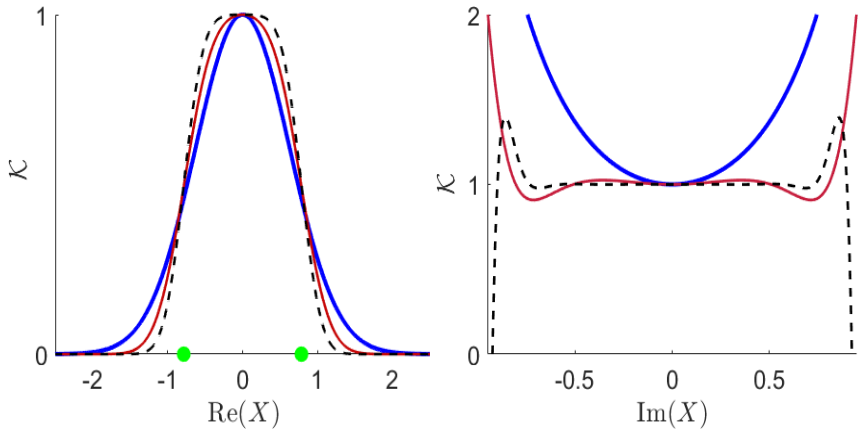


(a) (b)

Figure 2: Curvature profiles for three different sets of parameter values used in examples later. (a) curvature $\mathcal{K}(X)$ as a function of real $X$; in each case the profile is scaled to have a maximum value $\mathcal{K}_{\max} = \mathcal{K}(0) = 1$ here. Part (b) shows a section of the curvature profiles along the imaginary $X$-axis: this will be useful to understand the dynamics of complex orbits in later sections. (Blue thick solid curves correspond to $X^* = 0.42$ and $\delta X = 0.8136$, red thin solid curves to $X^* = 0.7776$ and $\delta X = 0.42$ and black dashed curves to $X^* = 0.7853$ and $\delta X = 0.2928$).

The curvature along the imaginary $X$ axis, plotted in part (b) of Fig. 2, will play a significant role in understanding the dynamics of complex orbits controlling reflection and transmission by tunnelling. For each of the three profiles shown, there is a local minimum in the imaginary direction. In the case of the flatter profiles shown in red and especially black, however, this local minimum is rather shallow and the profile is seen to oscillate, with growing amplitude, within the window plotted. (In fact even for the profile shown in blue the profile oscillates further along the imaginary axis, outside of the window plotted.) This feature becomes important in the treatment of complex rays in later sections.

We next describe explicit dispersion relations obtained in scaled variables, using the same material properties as in [6], that is, $\nu = 0.28$, $E = 195$ GPa and $\rho = 7700$ kg/m$^3$, for which $c = \sqrt{E/\rho} = 5032$ms$^{-1}$. Then, for example, $\mathcal{K}_{\max} = 1$ and $H = 6 \times 10^{-4}$ is achieved for a shell with thickness 0.5mm and maximum radius of curvature 0.833m, while a frequency of $f = \omega/(2\pi) = 1009$Hz results in a scaled frequency $\Omega = 1.05$.

Figure 3 shows corresponding level sets $D' = 0$ defined in the $(K_x, K_y)$ plane for two fixed values of scaled curvature $\mathcal{K}$ and for two values of $\Omega$: an example with $\Omega > 1$ is shown in (a) and an example with $\Omega < 1$ is shown in (b). In each case the dashed lines are for the flat limit $\mathcal{K} = 0$, for which the level set consists of three concentric circles. The outermost level curve corresponds to the bending mode, the middle level curve corresponds to shear waves and the innermost to pressure waves. In this limit, the wave veloc-

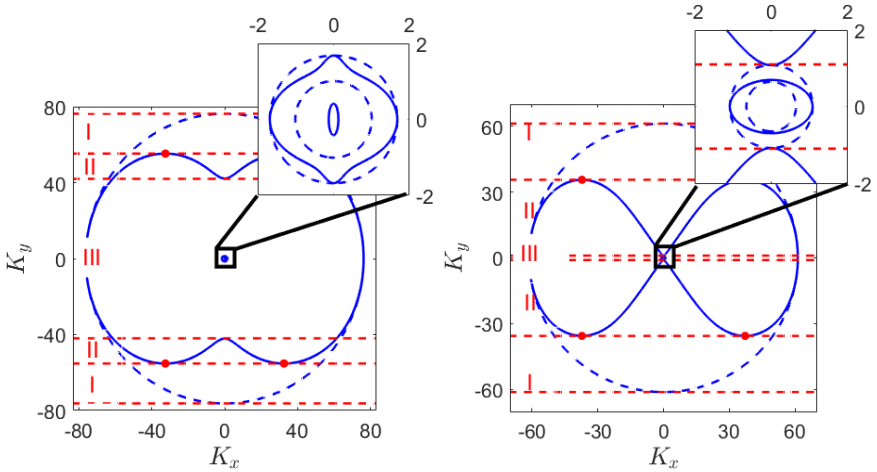


Figure 3: Dispersion curves, represented by level curves $D' = 0$ in the $(K_x, K_y)$-plane and for fixed $X$ are illustrated: an example with $\Omega > 1$ is shown in (a) and an example with $\Omega < 1$ is shown in (b). In each case, the blue dashed curves represent isotropic dispersion relations for the limit of a flat plate; the outer circle corresponds to bending modes, the middle circle (see inset) to shear modes and the smallest circle (see inset) represents pressure modes. The solid blue lines represent dispersion relations achieved for the maximum value $\mathcal{K}_{\max} = 1$ of the curvature profiles in Sec. 2.4. In (a), we identify three regions according to how incoming rays are reflected or transmitted by the curved region: rays with $K_y \in$ I are reflected and with those with $K_y \in$ II and III are transmitted. Incident waves in region II may experience resonant tunnelling, whereas those in region III do not. We also identify by red dots the values of $K_y$ connecting to fixed points of the system as explained in more detail in Sec. 2.5.

ity of each mode is independent of the direction of propagation and we note that, for the parameter values chosen here, the bending wavenumber is significantly greater than the two in-plane wavenumbers (see inset). As curvature increases, the circular symmetry of the flat limit is increasingly broken and, if the curvature is large enough, the bending component of the level set becomes non-convex. This transition corresponds to the green curve in Fig. 4. The case illustrated in Fig. 3a, for which $\Omega = 1.05$ and $\mathcal{K}_{\max} = 1$, shown by solid curves, is beyond this transition. If $\mathcal{K}_{\max}/\Omega > 1$ then the dispersion curves undergo a second transition (blue curve in Fig. 4) as the maximum of $\mathcal{K}(x)$ is approached. Here the bending curves collide with those for the in-plane modes and the level set develops a more complex structure for $(K_x, K_y)$ near $(0, 0)$, as seen in Fig. 3(b), for example.

In the following we restrict our attention to rays approaching the curved region in the bending mode, corresponding to the outermost level curves in Fig. 3. As such rays approach the curved region, the wave vector $(K_x, K_y)$ must stay on the deforming level set $D' = 0$, while $K_y$ remains fixed. To understand the possible outcomes, we identify three regions for the case $\mathcal{K}_{\max}/\Omega < 1$, labelled I, II and III, in Fig. 3a. A ray starting in region I

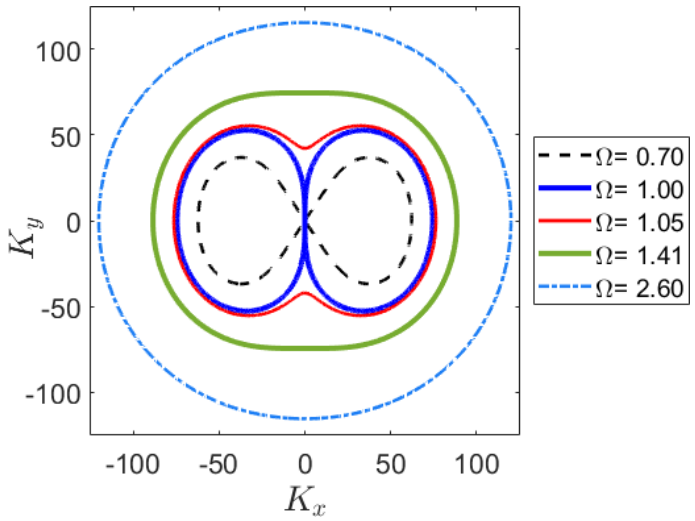


Figure 4: Level curves of the simplified Hamiltonian in (10) are plotted in scaled coordinates for a range of values of scaled frequency $\Omega$. These simplified dispersion curves do not capture the more complicated structure around $(0,0)$, as expanded in insets of Fig. 3, but provide a good description of them everywhere else in the $(K_x, K_y)$-plane.

does not have a compatible wave vector at the point of maximum curvature, which is an analogue of a "forbidden region" in quantum-mechanical scattering. Here the value of $K_y$ is large enough that the corresponding ray is deflected by the curved region and reflected back to the flat plate section from which it came. Rays starting in regions II and III do have compatible wave vectors at the point of maximum curvature: for these rays the value of $K_y$ is small enough that they can reach the region of maximum curvature and are transmitted to the other side. The difference between regions II and III is that in region II new compatible solutions $(K_x, K_y)$ appear as the level set is deformed: these new solutions are not directly accessible to rays arriving from the flat region but instead define trapped modes localised in the region of maximal curvature. The existence of such trapped modes have also been investigated by Gridin *et al.* [24]. In region III there are no such trapped modes. In the case $\mathcal{K}_{\max}/\Omega > 1$, illustrated in Fig. 3(b), region III has shrunk to a small gap in which all components of the dispersion curve interact for $(K_x, K_y)$ near $(0,0)$.

Our focus here is on the transition between regions I and II, where corresponding incident plane waves transition from being completely reflected to being completely transmitted. Although there is near complete transmission in region II, for some incident angles the trapped modes may locally mediate peaks in transmission in analogy to resonant tunnelling in quantum mechanics [25]. There are no such trapped modes in region III and therefore no resonant tunnelling. Although here there is still some small fraction of incident energy reflected for rays with $|K_y| \ll K_B$, this is typi-

cally so small that it is in practical terms unimportant. Therefore, although the simplified Hamiltonian (10) does not capture the structure of the dispersion curves near the origin of the $(K_x, K_y)$ plane, as shown in the insets of Fig. 3, it does give a good description of the dispersion curves around the transition between regions I and II and can be used as a basis to understand the resonant tunnelling calculations to follow. Contours of this simplified Hamiltonian are illustrated using scaled coordinates in Fig. 4. Note that the ring frequency provides a typical scale for the frequency range in which curvature effects are important: it is $O(1)$ in the scaled variables used here. For example, for the material parameters chosen in the illustration above, the general expression for it,[26]

$$\Omega_{\text{ring}} = \frac{1}{\sqrt{1-\nu^2}},$$

takes the value $\Omega_{\text{ring}} = 1.042$ .

*2.5. Phase portrait for bending rays*

In this subsection we present the phase portrait obtained in the $(X, K_x)$ plane from the scaled Hamiltonian in (9).

Figure 5 shows topologically distinct trajectories for the same parameter values as used in Fig 3. Each of these trajectories in the phase plane is a level curve defined by $D'(X, K_x; K_y, \Omega) = 0$. We fix $\Omega$ throughout and vary $K_y$ as an initial condition to obtain different contours. Depending on $K_y$, rays approaching the curved part of the plate are reflected, transmitted or approach a fixed point along a separatrix. These correspond respectively to rays arriving from the flat limit in regions I, II$\cup$III or the boundary between regions I and II in Fig. 3.

Rays approaching the curved region with sufficiently small values of $K_y$, in regions II or III in Fig. 3, are transmitted to the flat asymptotic region on the other side of the bend: rays of this type are labelled A in Figure 5. As the magnitude of $K_y$ approaches a threshold value $K_y^\sharp$, corresponding to the boundary between I and II in Fig. 3, the incident ray approaches a separatrix orbit labelled B in the phase plane of Figure 5. The corresponding ray paths form the stable and unstable manifolds of a fixed point in the phase plane. These form analogues of dividing surfaces used in chemical reaction theory to divide reactants from products [27]. The fixed point represents a trajectory moving along the line $X = 0$, see Fig. 5b. When $|K_y| > K_y^\sharp$, rays are deflected by the curved part of the plate: these are labelled C in Fig. 5. When $K_y^* < |K_y| < K_y^\sharp$, where $K_y^*$ corresponds to the boundary between regions II and III in Fig. 3, there are also topologically distinct orbits labelled D in Fig. 5; these orbits are closed in the $(X, K_x)$ phase plane. The corresponding ray paths are trapped in the region of the bend and oscillate along it as shown in Fig. 5(c). They are related to trapped bending modes to be

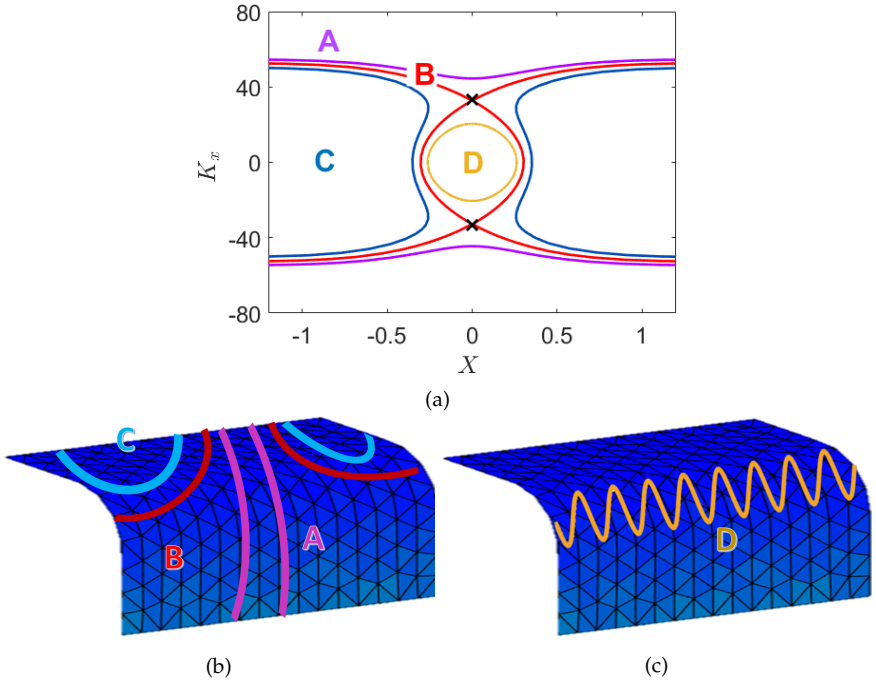


Figure 5: (a) Ray dynamics in a phase plane corresponding to a bending mode moving across a curved plate with the curvature profile shown in Fig. 2 (blue line); the magenta curve (A) is an example of a transmitted ray crossing the curved region; the red curve (B) corresponds to the ray approaching the fixed point thus forming a separatrix in the phase plane; the blue curve (C) represents a reflected ray; the closed yellow curve (D) shows a trapped ray oscillating along the curved part of the plate. The black crosses signify the fixed points at coordinates $(X, K_x; K_y) = (X, K_x^\sharp; K_y^\sharp)$. (b), (c) Typical ray paths are shown (schematically) on the curved plate using the same colour codes as in (a).

discussed in Section 3, see also [24]. These trapped rays cannot be reached from initial conditions in the flat regions of the plate. Incoming bending waves can couple into these trapped modes evanescently and these orbits play an important role in the "resonant tunnelling" mechanisms as set out in Section 3.

The key dividing structures in Fig. 5 are thus the hyperbolic fixed points (denoted by black crosses in Fig. 5a) at the threshold values $K_y = \pm K_y^\sharp$ and their corresponding stable and unstable manifolds shown as red curves. The coordinates of the fixed points $(X = 0, K_x = \pm K_x^\sharp)$ can be determined by imposing the conditions

$$D'(X = 0, K_x^\sharp; K_y^\sharp, \Omega) = 0 \quad \text{and} \quad \frac{\partial D'}{\partial K_x}(X = 0, K_x; K_y^\sharp, \Omega)\bigg|_{K_x = K_x^\sharp} = 0 \quad (13)$$

on the scaled Hamiltonian in (9). Although the exact solutions of the fixed point condition (13) can not be given in closed form in general, we can find approximate solutions using the Hamiltonian (10). Noting that $\partial D''/\partial K_x =$

$0 \Leftrightarrow \partial D''/\partial K = 0$ (at fixed $K_y$), the second of these conditions then implies

$$(K_x^\sharp)^2 + (K_y^\sharp)^2 = \frac{1}{\sqrt{2}} K_B^2 \left(1 + O\left(\frac{1}{H}\right)\right)$$

while the first yields

$$\left(K_y^\sharp\right)^2 = \frac{\Omega}{2\mathcal{K}_{\max}} K_B^2 \left(1 + O\left(\frac{1}{H}\right)\right).$$

Note, however, that the phase portrait in Fig. 5 has been constructed using the full Hamiltonian $D'(X, K_x; K_y, \Omega)$ in (9) and not the approximate Hamiltonian $D''(X, K_x; K_y, \Omega)$ in (10).

It is geometrically simpler to characterise incoming rays by an asymptotic angle of arrival

$$\theta_0 = \arcsin \frac{K_y}{K_B}$$

rather than wavenumber component $K_y$. We denote in particular by $\theta_0^\sharp$ the asymptotic angle of arrival of the separatrix orbit approaching the hyperbolic fixed point. From the preceding discussion this can be approximated by

$$\theta_0^\sharp = \arcsin \sqrt{\frac{\Omega}{2\mathcal{K}_{\max}}} \left(1 + O\left(\frac{1}{H}\right)\right).$$

An analysis based solely on the presented phase portrait would thus suggest that waves are predominantly reflected when $\theta_0 > \theta_0^\sharp$ and transmitted when $\theta_0 < \theta_0^\sharp$. Modification of this simple ray picture based on tunnelling effects are presented in the next section.

## 3. Transmission and reflection of bending waves: resonant tunnelling

We describe next how complex ray solutions can be used to describe transmission and reflection near the critical angle $\theta_0^\sharp$.

### *3.1. Overview*

To give an overview over the features to be described in detail later, we show the reflection and transmission coefficients, that is, the reflected and transmitted power as a fraction of the incident power of a plane wave arriving at the bend, as a function of the incident angle $\theta_0$ in Fig. 6. The calculations are done for the curvature profile shown as blue curves in Fig. 2. We compare numerical solutions of the full wave problem (3) (blue and red curves) with approximations that are to be developed in the remainder

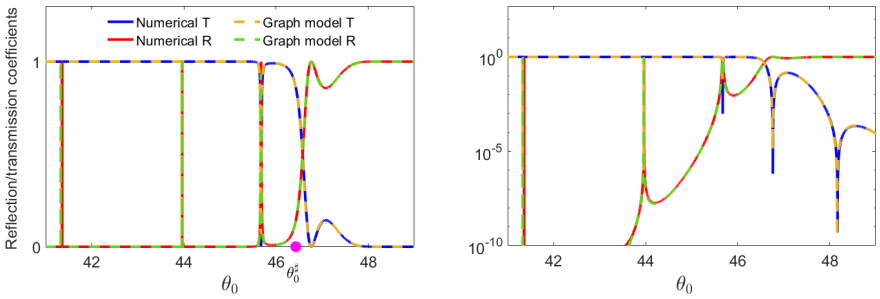


Figure 6: The fractions of transmitted (blue and yellow) and reflected (red and green) wave intensities are shown as a function of incident angle for a plane wave approaching the curved region from the flat limit using (a) a linear scale and (b) a log scale. Solid lines represent a full wave calculation using Eq. (3) and following [6]; dashed lines represent the approximations described in the text. The critical angle here is $\theta_0^\sharp = 46.4^\circ$ and the calculations have been done for the parameter values given in Sec. 2.4 and for the curvature profile shown in blue in Fig. 2.

of this paper (green and yellow dashed curves). For the full-wave solution, we apply a finite difference scheme as described in [6].

The main features are consistent with the ray-dynamical picture outlined in the previous section. For incoming angles $\theta_0 < \theta_0^\sharp$ (with $\theta_0^\sharp = 46.4^\circ$ here), the transmission coefficient is close to unity and the reflection coefficient is small. In line with Fig. 5, the corresponding rays (of type A) all pass over the curved region of the shell. Above this threshold, when $\theta_0 > \theta_0^\sharp$, the transmitted wave amplitude falls to zero: this is again consistent with Fig. 5, where the corresponding rays (of type C) are all deflected by the curved region.

The results in Fig. 6 deviate in two important ways from the simple ray picture sketched in the previous section, however. First, there is a transition region near the critical angle $\theta_0^\sharp$ in which the transmission and reflection coefficients change smoothly rather than discontinuously as a function of $\theta_0$. Second, at angles below this transition region, there are sharp resonances which are related to resonant tunnelling facilitated by the trapped orbits of type D in Fig. 5. Both of these features are explained quantitatively in the next sections by extending the ray analysis to use *complex rays*.

### *3.2. A graph model using complex rays*

In the following, we provide a complex-ray analysis of the transmission and reflection coefficients such as plotted in Fig. 6. In the quasi one-dimensional case here, this can be done most efficiently in a graph model based on the main features of the phase-space shown in Fig. 5 and, including transitions due to complex orbits leading to tunnelling corrections, in Fig. 7. The orbits shown in Fig. 7a are the dominant dynamical features

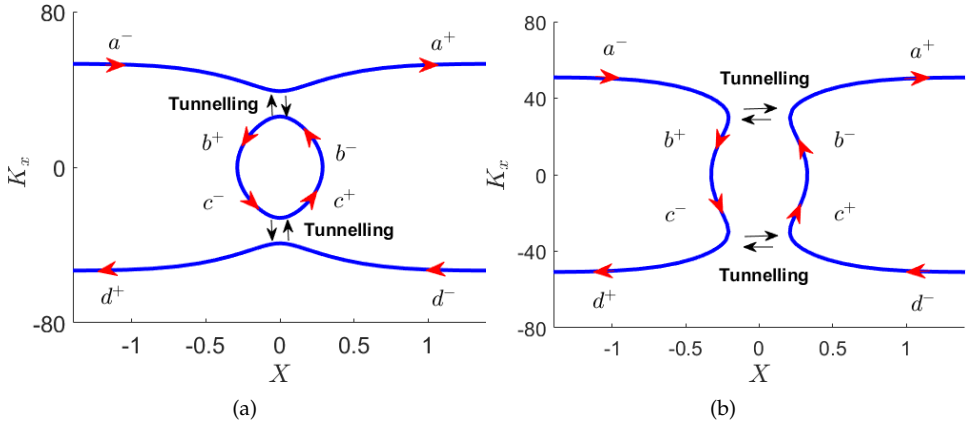


Figure 7: Phase space dynamics relevant for resonant tunnelling.

describing the behaviour below the critical point, for which $\theta_0 < \theta_0^\sharp$. Fig. 7b describes the behaviour for $\theta_0 > \theta_0^\sharp$.

The calculations in this section borrow from two approaches in the areas of wave chaos and semiclassical approximation of quantum mechanics. The first is the use of graph models (or "quantum graphs"), in which wave solutions transported along networks of bonds are connected at vertices by local scattering matrices. Imposing global consistency of such locally connected solutions leads to explicit solutions for important features of the system as a whole, such as scattering matrices and resonance conditions. Ref [28] provides a good overview of the most important results and concepts in this context. Second is the use of uniform asymptotic approximation to characterise the connection of local WKB solutions across hyperbolic fixed points, where primitive WKB approximation breaks down. A detailed exposition of these so-called connection formulae that is valid for the effectively one-dimensional context needed here can be found in the classic review article [29]. We also note that this topic has had renewed attention in recent years in the context of chemical reaction rates [27], where transport across phase space bottlenecks is treated by similar methods, extended to more general Hamiltonians and higher dimensions: although these reaction-rate problems are physically very distinct, their phase-space geometry and WKB approximation are very similar to the problem at hand [30]. We will not give a detailed re-derivation of the required results in this paper but simply quote the most important equations from these references.

Each orbit in phase space can be used to define an approximate solution of WKB type matching plane waves as $x \to \pm\infty$ with corrections due to the curved region near $x = 0$. We write the full wave solution as linear combinations of these WKB solutions in each region with corresponding amplitudes $(a^\pm, b^\pm, c^\pm, d^\pm)$ as denoted in Fig. 7. For example, $a^-$ denotes

the amplitude of a wave incoming from the left and $a^+$ the amplitude of a corresponding outgoing wave to the right following transmission, whereas $d^+$ denotes a corresponding reflection amplitude.

Our aim is to calculate a scattering matrix connecting these amplitudes, defined so that

$$\begin{bmatrix} a^+ \\ d^+ \end{bmatrix} = \begin{bmatrix} t_{\text{tot}} & r_{\text{tot}} \\ r_{\text{tot}} & t_{\text{tot}} \end{bmatrix} \begin{bmatrix} a^- \\ d^- \end{bmatrix} \equiv \sigma_{\text{tot}} \begin{bmatrix} a^- \\ d^- \end{bmatrix}. \tag{14}$$

The transmission and reflection coefficients such as those shown in Fig. 6 are then obtained using

$$T = |t_{\text{tot}}|^2 \quad \text{and} \quad R = |r_{\text{tot}}|^2.$$

The scattering process can be schematically displayed in a graph model as shown in Fig. 8. We find the total scattering matrix $\sigma_{\text{tot}}$ by subdividing the problem into local scattering problems and associated node scattering matrices $\sigma_{\text{node}}$.

We first treat scattering at the nodes of the graph in Fig. 8 corresponding to the region in phase space surrounding either of the two hyperbolic fixed points. Wave amplitudes connecting local WKB solutions approaching and leaving the upper fixed point in Fig. 7 can be related in the form

$$\begin{bmatrix} a^+ \\ b^+ \end{bmatrix} = \begin{bmatrix} t_{\text{node}} & r_{\text{node}} \\ r_{\text{node}} & t_{\text{node}} \end{bmatrix} \begin{bmatrix} a^- \\ b^- \end{bmatrix} \equiv \sigma_{\text{node}} \begin{bmatrix} a^- \\ b^- \end{bmatrix}. \tag{15}$$

We obtain by symmetry for the lower fixed point

$$\begin{bmatrix} c^+ \\ d^+ \end{bmatrix} = \sigma_{\text{node}} \begin{bmatrix} c^- \\ d^- \end{bmatrix}. \tag{16}$$

Explicit formulas can be given for the matrix elements of the node scattering matrix $\sigma_{\text{node}}$ based on a uniform WKB treatment of wave propagation near a hyperbolic fixed point, as discussed below.

Wave transport along the bonds between nodes in the graph is achieved by applying a simple phase shift determined by the optical phase length of the corresponding ray segment. By matching the local WKB solutions between the upper and lower nodes we may write

$$\begin{bmatrix} b^- \\ c^- \end{bmatrix} = \begin{bmatrix} 0 & -\mathrm{i}\,\mathrm{e}^{\mathrm{i}S} \\ -\mathrm{i}\,\mathrm{e}^{\mathrm{i}S} & 0 \end{bmatrix} \begin{bmatrix} b^+ \\ c^+ \end{bmatrix} \equiv \sigma_X \begin{bmatrix} b^+ \\ c^+ \end{bmatrix}, \tag{17}$$

where $S$ denotes a phase integral (or action) of an orbit passing from the upper to the lower node or vice versa. The details of the transformation $\sigma_X$ depends on the phase conventions used to write each of the local WKB solutions. The factor $(-\mathrm{i})$ is due to connecting WKB solutions across turning points between nodes [29].

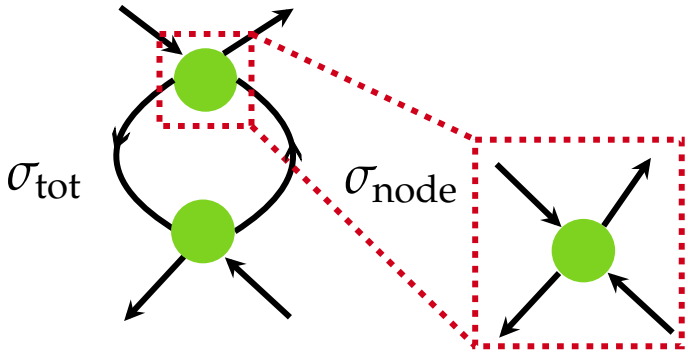


Figure 8: Schematic representation of the graph model.

We can use (17) to eliminate the amplitudes $(b^{\pm}, c^{\pm})$ from the total scattering problem and write (14) in the form

$$\sigma_{\text{tot}} = t_{\text{node}} I + r_{\text{node}} \sigma_X \frac{1}{1 - t_{\text{node}} \sigma_X} r_{\text{node}},$$

where $I$ denotes the identity matrix. The treatment suggested here is in fact a special case of constructing a scattering matrix for a wave dynamics on general graphs [28]. The total scattering matrix can also be expressed as a sum over all possible paths between branches approaching and leaving the nodes. Written explicitly in terms of matrix elements, this matrix equation leads to the following relations,

$$r_{\text{tot}} = \frac{-\mathrm{i}\, r_{\text{node}}^2 \mathrm{e}^{\mathrm{i}S}}{1 + t_{\text{node}}^2 \mathrm{e}^{2\mathrm{i}S}} \tag{18a}$$

and

$$t_{\text{tot}} = t_{\text{node}} \left[ 1 - \frac{r_{\text{node}}^2 \mathrm{e}^{2\mathrm{i}S}}{1 + t_{\text{node}}^2 \mathrm{e}^{2\mathrm{i}S}} \right] = t_{\text{node}} \left[ \frac{1 + (t_{\text{node}}^2 - r_{\text{node}}^2) \mathrm{e}^{2\mathrm{i}S}}{1 + t_{\text{node}}^2 \mathrm{e}^{2\mathrm{i}S}} \right] \tag{18b}$$

for total reflection and transmission, respectively.

Resonant tunnelling occurs when the denominator becomes small, that is,

$$1 + t_{\text{node}}^2 \mathrm{e}^{2\mathrm{i}S} \approx 0.$$

Below the critical angle $\theta_0^{\sharp}$, we find that transmission across a node is almost total, so that $t_{\text{node}} \approx 1$ and such resonances arise near parameters for which

$$S = \left( n + \frac{1}{2} \right) \pi,$$

where $n$ is integer. This Bohr-Sommerfeld type quantisation condition is satisfied by parameter values near those supporting a trapped, resonant

mode confined to the region of maximum curvature and associated with orbits of type D in Fig. 5. Incoming waves couple into such trapped modes at resonance and show enhanced reflection (and correspondingly depressed transmission), as seen in the numerical calculation of Fig. 6. We show in the next section that the results described here allow a detailed quantitative comparison of such resonant tunnelling effects.

*3.3. Local scattering matrices*

In the following, we will derive the local scattering matrices $\sigma_{\mathrm{node}}$ and $\sigma_X$, starting with $\sigma_{\mathrm{node}}$. The problem of transmission and reflection of local WKB solutions around a hyperbolic fixed point has been extensively studied in the context of quantum mechanics. In its simplest form, it is understood by solving the problem of transmission across a quadratic potential barrier [29], but can also be treated by using more general transformations of phase-space coordinates around generic hyperbolic fixed points as we encountered here: see [27] for a discussion of phase space geometry and [30] for a corresponding discussion from the point of view of WKB approximation, for example.

The main ingredient is to find a complex periodic orbit $\gamma_{\mathrm{i}}$ connecting disconnected branches of the level curves illustrated in Fig. 7. This is obtained by solving Hamilton's equations (7) while letting the "time" variable run along a contour in the complex plane. One can show that there are periodic solutions connecting each pair of branches near a hyperbolic fixed point [30]. These are illustrated in Figs. 9a-9b for $K_y < K_y^\sharp$ and in Figs. 10a-10b for $K_y > K_y^\sharp$. One finds in this case that the period in complex time is in fact imaginary, and so is the corresponding orbit action, which we denote

$$\oint_{\gamma_{\mathrm{i}}} K_x \mathrm{d}X = 2\mathrm{i}\Theta, \tag{19}$$

(where $\Theta$ is in fact a function of the parameters $K_y$ and $\Omega$). By choosing the imaginary-time contour to move *downwards* in the complex plane, the imaginary action $\Theta$ is negative when $K_y > K_y^\sharp$ and positive when $K_y < K_y^\sharp$ [30]. This leads to near complete transmission for $K_y < K_y^\sharp$ and near complete reflection for $K_y > K_y^\sharp$ as discussed in more detail below.

Note that any such complex periodic orbit is one of a continuous family of equivalent orbits, so that collectively they define a two-dimensional manifold. A real starting point can be displaced continuously along the (real) level curve of the Hamiltonian function, corresponding to the blue curves in Fig. 7. Subsequent evolution in imaginary time will generate different periodic curves on a complexified level set $D'(X, K_x; K_y, \Omega) = 0$ (which defines a manifold of two real dimensions in complexified phase space), but each of these periodic curves will have the same period and imaginary action $\Theta$ as a consequence of Cauchy's theorem.

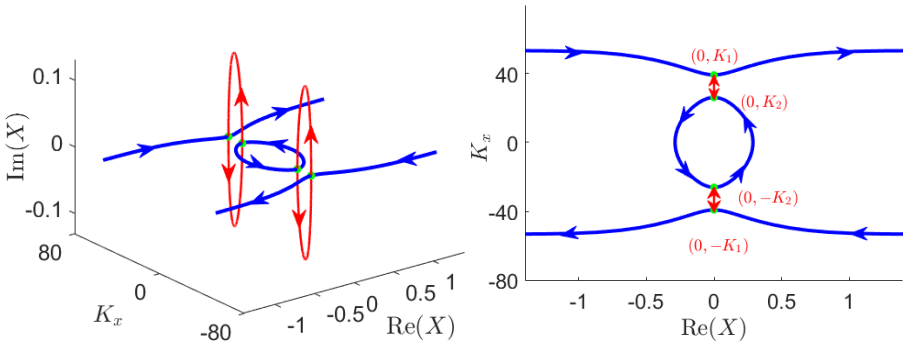


Figure 9: Real and complex (tunnelling) orbits are shown for the case $K_y < K_y^\sharp$. In (a) we provide a 3D representation in which a degree of freedom corresponding to the imaginary part of $X$ is included; in (b) the corresponding projection onto the real phase plane is shown. Red curves show examples of tunnelling orbits of imaginary period: for these orbits, real initial conditions can be found, indicated by green dots, from which integration in imaginary time leads to periodic evolution largely confined to $\mathrm{Re}(K_x)$ and $\mathrm{Im}(X)$. There is also a separate real periodic orbit corresponding to the closed blue curve.

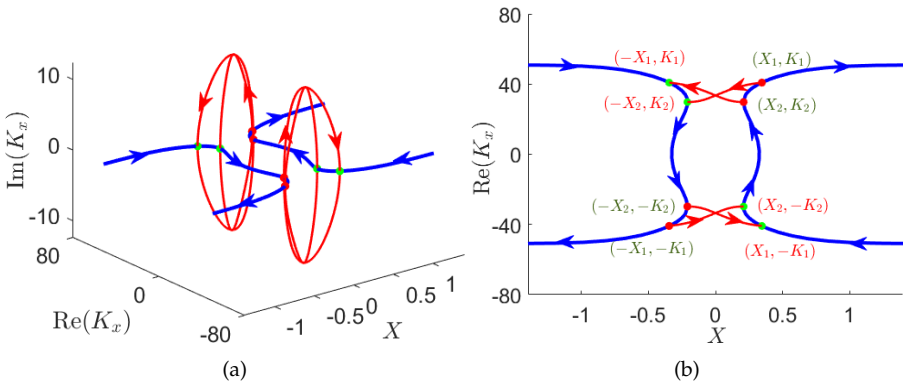


Figure 10: Real and complex (tunnelling) orbits for the case $K_y > K_y^\sharp$. The format is similar to Fig. 9a-9b except that the 3D plot is obtained by including the imaginary part of $K_x$ rather than of $X$. As with Fig. 9a-9b, the red curves show examples of tunnelling orbits of imaginary period, but note that here dynamics is predominantly in components $\mathrm{Re}(X)$ and $\mathrm{Im}(K_x)$ rather than $\mathrm{Re}(K_x)$ and $\mathrm{Im}(X)$. In contrast to Fig. 9a-9b, where symmetry of reflection in $X$ suggests a particular real initial condition for each tunnelling orbit, here there are many, equally plausible real initial conditions. For example, imaginary-time evolution from the turning point $(X_2, K_2)$ on the right first returns to the real phase plane at coordinates $(-X_1, K_1)$, which is not a turning point. Conversely evolution from $(X_1, K_1)$, which is not a turning point, first returns to the real phase plane at turning point $(-X_2, K_2)$.

With an appropriate choice of phase convention for local WKB solutions, the local reflection and transmission coefficients can then be expressed in the forms [29, 30]

$$r_{\text{node}} = \frac{-\mathrm{i}\mathrm{e}^{-\mathrm{i}\delta}}{\sqrt{1+\mathrm{e}^{-2\Theta}}}, \tag{20a}$$

and

$$t_{\text{node}} = \frac{\mathrm{e}^{-\Theta-\mathrm{i}\delta}}{\sqrt{1+\mathrm{e}^{-2\Theta}}}, \tag{20b}$$

where

$$\delta(\Theta) = \frac{\Theta}{\pi}\log\left|\frac{\Theta}{\pi\mathrm{e}}\right| + \arg\Gamma\left(\frac{1}{2}-\frac{\mathrm{i}\Theta}{\pi}\right). \tag{21}$$

Note that $\sigma_{\text{node}}$ is unitary and that, in particular,

$$|r_{\text{node}}|^2 + |t_{\text{node}}|^2 = 1.$$

Note also that the derivation of this result assumes that the fixed point in question is of generic hyperbolic type [27, 30] which necessitates that the maxima of the curvature profiles in Fig. 2 are quadratic. This is unambiguously true for the curvature profile represented by blue curves in Fig. 2. The maxima for the other profiles in Fig. 2, while being also strictly quadratic, are very shallow, so that effectively higher-order terms in a normal form representation [27] are in practice not negligible. The problem is therefore expected to be well described by these generic results only for extremely small values of the small parameter $H$ defined in (8). The approximations used here are therefore challenged by these examples but we will find nevertheless that there is qualitative consistency with the full-wave results, as described in the next section.

There is also a real periodic orbit $\gamma_{\text{r}}$, which defines a real action by

$$\oint_{\gamma_{\text{r}}} K_x \mathrm{d}X = 2S. \tag{22}$$

Below the threshold ($|K_y| < K_y^\sharp$), the closed orbit corresponds to the blue curves in Fig. 9a-9b. The action $S$ is then simply the area enclosed by the closed orbit in the real phase plane. It is this action $S$ that is used to define the matrix $\sigma_X$ in (17). A corresponding action can be obtained for $|K_y| > K_y^\sharp$ by a somewhat more complicated integration path involving segments of complex evolution but having overall a net real displacement in the complex time plane. For example, starting at the top right turning point $(X_2, K_2)$ in Fig. 10b and evolving in negative imaginary time first returns the trajectory to the real phase plane at $(-X_1, K_1)$. From there, evolution

in real time brings the orbit to the bottom left turning point at $(-X_2, -K_2)$. From here, evolution in positive imaginary time returns the trajectory to the real phase plane at $(X_1, -K_2)$ and subsequent evolution in real time brings the orbit back to its starting position at $(X_2, K_2)$. If the segments of the imaginary-time evolution are in opposite directions in the complex plane, the net action for this orbit is real, and defines $S$ through (22). Again as a result of Cauchy's theorem, this real action does not change if the integration path in the complex time plane is deformed, or alternative initial conditions are chosen.

## 4. Results

We first test the results of the the graph model described in the previous section for the curvature profile with a generic quadratic maximum represented by blue curves in Fig. 2a. A comparison of numerically calculated transmission and reflection fractions against the predictions of the graph model has already been shown in Fig. 6. We find in this case that there is detailed, qualitative and quantitative agreement between the graph models and full-wave numerical results. This agreement includes both the smooth transition across $\theta_0 = \theta_0^\sharp$ and the positions and shape of resonant scattering peaks for $\theta_0 < \theta_0^\sharp$. Above the transition, there is accurate reproduction of the zeros of the transmitted fraction, evident in the log plot of part (b).

We have also compared the results of the graph model to the flatter curvature profiles represented by red and black curves in Fig. 2, which have been designed to challenge the assumptions of the model and to test how it might fail. First, although these profiles have strictly-speaking quadratic maxima, these are in practice very shallow so that approximations Eqs. (20a-20b) would require extremely small values of the thickness parameter $H$ in order to be valid. Second, the $X$ coordinate of the tunnelling orbit shown in Fig. 9, which is for incidence below the transition angle, evolves along the imaginary axis. Therefore its dynamics uses the profiles shown in Fig. 2b. For the flatter profiles these show a shallow local minimum and then begin to oscillate as a function of $\mathrm{Im}(X)$ (the generic profile in blue also oscillates for large enough $\mathrm{Im}(X)$ but at scales that do not have impact on the calculations here). We will observe that this leads to bifurcations in the tunnelling orbit that qualitatively affect the reflection and transmission coefficients.

For the middle curvature profile (red curve), there is reasonable agreement across the transition region, as shown in Fig. 11, although this agreement is not as close as in Fig. 6. For the flattest profile (black curve in Fig. 2), the reflection and transmission coefficients show reasonable agreement above the transition (see Fig. 12b), but there are significant quantitative differences across the transition region. Here the second derivative of the curvature profile is so small at its peak that (20a-20b) do not adequately

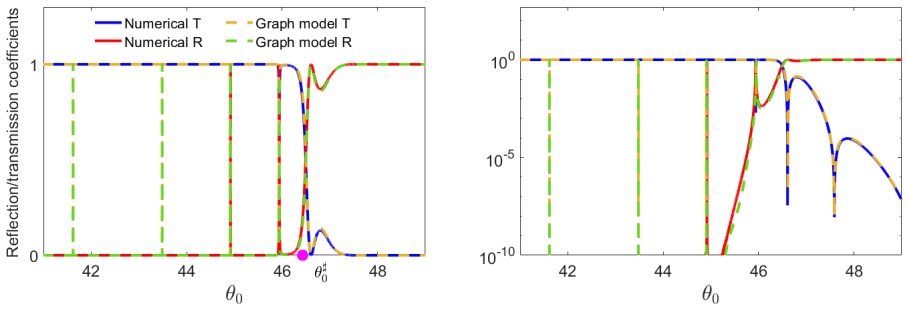


(a) (b)

Figure 11: Transmission and reflection coefficients shown here using the same conventions as in Fig. 6 but for the intermediate curvature profile represented by the red curve in Fig. 2. The agreement here is still very good, but compared to Fig. 6 small deviations are noticeable especially near $\theta_0 = \theta_0^\sharp$ due to the behaviour of the curvature profile around $X = 0$.

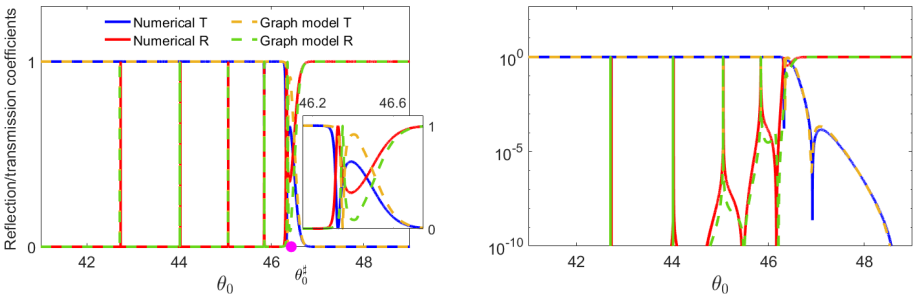


(a) (b)

Figure 12: Transmission and reflection coefficients shown here use the same conventions as in Fig. 6 but for the flattest curvature profile represented by a black curve in Fig. 2. Although quantitative agreement is poor across the transition region, there is qualitative similarity and features away from the transition are well reproduced.

describe the behaviour of $\sigma_{\text{node}}$ near the transition. Far enough above the transition, however, where $\Theta \gg 1$ and $\delta \approx 0$, the primitive approximations $r_{\text{node}} \approx -\mathrm{i}$ and $t_{\text{node}} \approx \mathrm{e}^{-\Theta}$ are valid and agreement is better.

Below the transition (where $\theta_0 < \theta_0^\sharp$), there are even starker deviations, which arise due to the oscillation of $\mathcal{K}(X)$ along the imaginary axis (see Fig. 2b). The tunnelling orbit undergoes a bifurcation at an incident angle $\theta_0^\flat$ below $\theta_0^\sharp$ (and in fact $\theta_0^\flat$ is quite near $\theta_0^\sharp$ for the flattest curvature profile). This bifurcation is illustrated in Fig. 13 for the intermediate curvature profile. In Fig. 13b we show a phase portrait obtained by plotting level curves $D' = 0$ of the Hamiltonian (as $\theta_0$ or $K_y$ are varied) in a plane with axes $(K_x, \mathrm{Im}(X))$ (where symmetries mean that $D'$ remains real): when $\theta_0 = \theta_0^\flat$ the corresponding level curves form a separatrix dividing a short tunnelling orbit of the form seen in Fig. 9 from a more complicated orbit with an extra lobe shown by the red curves in In Fig. 13a. Here the complex orbit with the smallest imaginary action is obtained by taking a shortcut across the real orbit shown in green in Fig. 13a. It is the action of this truncated complex orbit that dominates tunnelling rates when $\theta_0 < \theta_0^\flat$.

The detailed behaviour of such complex phase portraits depends critically on the behaviour of the curvature profile along the imaginary $X$ axis. This behaviour can be significantly different even for profiles that look quite similar along the real axis. We therefore do not propose to give a systematic accounting of such additional structure in this paper: treatment of conversion rates around the angle $\theta_0^\flat$ at which the shortcut appears would require an analysis at least as complicated as that behind (20a-20b) and might then need to be revisited for each new family of curvature profiles treated, if their behavior along the imaginary $X$ axis is different. Instead we simply provide a simplified calculation to demonstrate in broad terms that such bifurcations are able to explain what is observed for the curvature profiles in Fig. 2.

Far enough below the transition, where $\Theta$ is negative and large in magnitude and $\delta \approx 0$, the primitive approximations $r_{\text{node}} \approx -\mathrm{i}\mathrm{e}^{\Theta}$ and $t_{\text{node}} \approx 1$ are valid. In plotting the results of the graph model in Figs. 11 and 12, we have replaced $\mathrm{e}^{\Theta}$ by $\mathrm{Re}(\mathrm{e}^{\Theta})$ for $\theta_0 < \theta_0^\flat$. Because $\mathrm{Re}(\Theta) \neq 0$ here, this is an oscillatory function of $\theta_0$ and has zeroes, for example. These oscillations and zeroes agree well with those observed in calculations from the full wave model, seen in Figs. 11b and 12b. Such bifircations of the complex tunnelling orbit therefore provide an means of understanding more complex behaviour in scattering from plate bends.

## 5. Conclusion

We have provided an analysis of the transition between complete reflection and complete transmission of bending waves incident on a curved section of a thin shell. The analysis is based on complex ray theory and

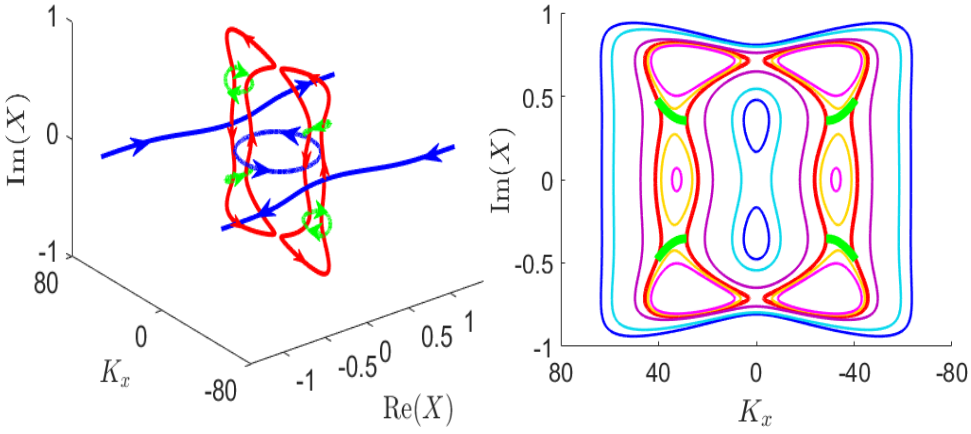


Figure 13: Real and complex orbits for the second curvature profile (red line in Fig. 2) are shown for the case $K_y < K_y^\sharp$. Some of the complex orbits with real initial conditions ($X = 0$) change geometry due to bifurcations. In (a) the bifurcation occurs close to $(\mathrm{Re}(X), \mathrm{Im}(X), K_x) = (0, \pm 0.36, 38)$; here, the red curves show examples of tunnelling orbits with imaginary action (long orbits) and the green curves show examples of tunnelling orbits with real action. In (b), the phase-space $(K_x, \mathrm{Im}(X))$ of complex orbits with imaginary action for the second curvature profile are shown.

extends the treatment based on real ray dynamics provided in [5, 6]. These results allow us to model a smooth transition where complete transmission turns to complete reflection as an incidence angle increases, and also to model resonance effects where reflection is enhanced by coupling to local modes trapped in the curved region of the plate.

For a generic curvature profile with a simple quadratic maximum, the analysis works extremely well not only in explaining the smooth transition between complete reflection and complete transmission, but also reproduces in detail phenomena such as reflection mediated by trapped resonances (resonant tunnelling).

We have also compared the predictions of the model to scattering properties of curvature profiles with flat maxima. Here the assumptions made to derive the model begin to fail and we observe quantitative deviations from its predictions. Nevertheless the model succeeds in describing qualitatively the reflection and transmission rates calculated numerically from a full wave treatment, including resonance positions and fluctuations in reflection and transmission rates arising due to bifurcations of the underlying complex orbit to more complicated forms.

**Acknowledgements**

We would like to thank Dr Sharad Jain and Dr David Chappell for helpful discussions. We also thank Romax Technology for financial support.

## References


[1] G. Tanner, Dynamical energy analysis—determining wave energy distributions in vibro-acoustical structures in the high-frequency regime, Journal of Sound and Vibration 320 (4) (2009) 1023 – 1038. doi:https://doi.org/10.1016/j.jsv.2008.08.032.
URL http://www.sciencedirect.com/science/article/pii/S0022460X08007487

[2] D. J. Chappell, G. Tanner, D. Löchel, N. Søndergaard, Discrete flow mapping: transport of phase space densities on triangulated surfaces, Proceedings of the Royal Society A: Mathematical, Physical and Engineering Sciences 469 (2155) (2013) 20130153. arXiv:https://royalsocietypublishing.org/doi/pdf/10.1098/rspa.2013.0153, doi:10.1098/rspa.2013.0153.
URL https://royalsocietypublishing.org/doi/abs/10.1098/rspa.2013.0153

[3] T. Hartmann, S. Morita, G. Tanner, D. J. Chappell, High-frequency structure- and air-borne sound transmission for a tractor model using dynamical energy analysis, Wave Motion 87 (2019) 132 – 150, innovations in Wave Modelling II. doi:https://doi.org/10.1016/j.wavemoti.2018.09.012.
URL http://www.sciencedirect.com/science/article/pii/S0165212518303913

[4] D. Chappell, D. Löchel, N. Søndergaard, G. Tanner, Dynamical energy analysis on mesh grids: A new tool for describing the vibro-acoustic response of complex mechanical structures, Wave Motion 51 (4) (2014) 589 – 597, innovations in Wave Modelling. doi:https://doi.org/10.1016/j.wavemoti.2014.01.004.
URL http://www.sciencedirect.com/science/article/pii/S0165212514000067

[5] N. Søndergaard, D. J. Chappell, G. Tanner, Tracking vibrational energy on curved shell structures in the mid-high frequency limit-a ray-tracing approach, Proceedings of Noise and Vibration-Emerging Technologies (NOVEM) 251 (1) (2015) 195–204.

[6] N. Søndergaard, D. J. Chappell, Ray and wave scattering in smoothly curved thin shell cylindrical ridges, Journal of Sound and Vibration 377 (2016) 155 – 168. doi:https://doi.org/10.1016/j.jsv.2016.05.019.
URL http://www.sciencedirect.com/science/article/pii/S0022460X16301328

[7] A. D. Pierce, Waves on Fluid-Loaded Inhomogeneous Elastic Shells of Arbitrary Shape, Journal of Vibration and Acoustics 115 (4) (1993) 384–390. arXiv:https://asmedigitalcollection.asme.org/vibrationacoustics/article-pdf/115/4/384/5825062/384_1.pdf, doi:10.1115/1.2930361.
URL https://doi.org/10.1115/1.2930361

[8] A. N. Norris, D. A. Rebinsky, Membrane and Flexural Waves on Thin Shells, Journal of Vibration and Acoustics 116 (4) (1994) 457–467. arXiv:https://asmedigitalcollection.asme.org/vibrationacoustics/article-pdf/116/4/457/5825116/457_1.pdf, doi:10.1115/1.2930449.
URL https://doi.org/10.1115/1.2930449

[9] G. Mikhasev, P. Tovstik, Localized Dynamics of Thin-Walled Shells, Chapman & Hall/CRC Monographs and Research Notes in Mathematics, CRC Press, 2020.
URL https://books.google.co.uk/books?id=SOreDwAAQBAJ

[10] J. Kaplunov, L. Yu Kossovich, E. Nolde, Dynamics of Thin Walled Elastic Bodies, Academic Press, London, 1998. doi:https://doi.org/10.1016/C2009-0-20923-8.
URL https://www.sciencedirect.com/book/9780080504865/dynamics-of-thin-walled-elastic-bodies

[11] V. Babich, A. Kiselev, Elastic Waves: High Frequency Theory, Chapman & Hall/CRC Monographs and Research Notes in Mathematics, CRC Press, 2018.
URL https://books.google.co.uk/books?id=TyJWDwAAQBAJ

[12] M. Razavy, Quantum Theory of Tunneling, WORLD SCIENTIFIC, 2003. arXiv:https://www.worldscientific.com/doi/pdf/10.1142/4984, doi:10.1142/4984.
URL https://www.worldscientific.com/doi/abs/10.1142/4984

[13] A. Shudo, Y. Ishii, K. S. Ikeda, Julia sets and chaotic tunneling: I, Journal of Physics A: Mathematical and Theoretical 42 (26) (2009) 265101. doi:10.1088/1751-8113/42/26/265101.
URL https://doi.org/10.1088%2F1751-8113%2F42%2F26%2F265101

[14] A. Shudo, Y. Ishii, K. S. Ikeda, Julia sets and chaotic tunneling: II, Journal of Physics A: Mathematical and Theoretical 42 (26) (2009) 265102. doi:10.1088/1751-8113/42/26/265102.
URL https://doi.org/10.1088%2F1751-8113%2F42%2F26%2F265102

[15] S. C. Creagh, N. D. Whelan, Complex periodic orbits and tunneling in chaotic potentials, Phys. Rev. Lett. 77 (1996) 4975–4979. doi:10.1103/

PhysRevLett.77.4975.
URL https://link.aps.org/doi/10.1103/PhysRevLett.77.4975

[16] O. Brodier, P. Schlagheck, D. Ullmo, Resonance-assisted tunneling, Annals of Physics 300 (1) (2002) 88 – 136. doi:https://doi.org/10.1006/aphy.2002.6281.
URL http://www.sciencedirect.com/science/article/pii/S0003491602962810

[17] J. Ankerhold, Quantum Tunneling in Complex Systems: The Semiclassical Approach, Vol. 224, Springer, 2007. doi:https://doi.org/10.1007/3-540-68076-4.
URL https://link.springer.com/book/10.1007/3-540-68076-4

[18] S. Keshavamurthy, P. Schlagheck, Dynamical tunneling: theory and experiment, CRC Press, 2011.

[19] S. C. Creagh, Tunnelling in multidimensional systems, Journal of Physics A: Mathematical and General 27 (14) (1994) 4969–4993. doi:10.1088/0305-4470/27/14/023.
URL https://doi.org/10.1088%2F0305-4470%2F27%2F14%2F023

[20] L. H. Donnell, Stability of thin-walled tubes under torsion, Tech. Rep. 479 (1933).
URL https://ntrs.nasa.gov/search.jsp?R=19930091553

[21] A. D. PIERCE, 2 - variational formulations in acoustic radiation and scattering, in: A. D. PIERCE, R. THURSTON (Eds.), Physical Acoustics, Vol. 22 of Physical Acoustics, Academic Press, 1993, pp. 195 – 371. doi:https://doi.org/10.1016/B978-0-12-477922-8.50007-8.
URL http://www.sciencedirect.com/science/article/pii/B9780124779228500078

[22] A. Leissa, Vibration of Shells, NASA SP, Scientific and Technical Information Office, National Aeronautics and Space Administration, 1973.
URL https://books.google.co.uk/books?id=VOb2l7gnNtcC

[23] M. S. Qatu, Recent research advances in the dynamic behavior of shells: 1989–2000, Part 2: Homogeneous shells , Applied Mechanics Reviews 55 (5) (2002) 415–434. arXiv:https://asmedigitalcollection.asme.org/appliedmechanicsreviews/article-pdf/55/5/415/6521403/415_1.pdf, doi:10.1115/1.1483078.
URL https://doi.org/10.1115/1.1483078

[24] D. Gridin, R. V. Craster, A. T. Adamou, Trapped modes in curved elastic plates, Proceedings of the Royal Society A: Mathematical,

Physical and Engineering Sciences 461 (2056) (2005) 1181–1197. arXiv:https://royalsocietypublishing.org/doi/pdf/10.1098/rspa.2004.1431, doi:10.1098/rspa.2004.1431.
URL https://royalsocietypublishing.org/doi/abs/10.1098/rspa.2004.1431

[25] D. Bohm, Quantum Theory, Dover books in science and mathematics, Dover Publications, 1989.
URL https://books.google.co.uk/books?id=-vhCqN2twGQC

[26] J. Gieras, C. Wang, J. Lai, Noise of Polyphase Electric Motors, Electrical and Computer Engineering, CRC Press, 2018.
URL https://books.google.co.uk/books?id=SUVuBwAAQBAJ

[27] T. Uzer, C. Jaffé, J. Palacián, P. Yanguas, S. Wiggins, The geometry of reaction dynamics, Nonlinearity 15 (4) (2002) 957–992. doi:10.1088/0951-7715/15/4/301.
URL https://doi.org/10.1088%2F0951-7715%2F15%2F4%2F301

[28] S. Gnutzmann, U. Smilansky, Quantum graphs: Applications to quantum chaos and universal spectral statistics, Advances in Physics 55 (5-6) (2006) 527–625. arXiv:https://doi.org/10.1080/00018730600908042, doi:10.1080/00018730600908042.
URL https://doi.org/10.1080/00018730600908042

[29] M. V. Berry, K. E. Mount, Semiclassical approximations in wave mechanics, Reports on Progress in Physics 35 (1) (1972) 315–397. doi:10.1088/0034-4885/35/1/306.
URL https://doi.org/10.1088%2F0034-4885%2F35%2F1%2F306

[30] S. C. Creagh, Semiclassical transmission across transition states, Nonlinearity 18 (5) (2005) 2089–2110. doi:10.1088/0951-7715/18/5/011.
URL https://doi.org/10.1088%2F0951-7715%2F18%2F5%2F011